PAPER

Check for updates

Bismuth nanoclusters on nitrogen-doped porous carbon nanoenzyme for cancer therapy†

Songjing Zhong,‡[a,b] Zeyu Zhang,‡[a,c] Yunchao Zhao,[a,c] Shaobo Wang,[a,c] Quanhong Hu[a,c] and Linlin Li ★[a,b,c]

Among the emerging cancer therapeutic methods, nanocatalytic therapy through the rational design of nanozymes is considered to be a promising strategy. However, high-performance nanozymes with the ability to catalyze the production of toxic substances to efficiently kill cancer cells are still highly desired. Herein, we fabricate bismuth nanoclusters loaded on nitrogen-doped porous carbon (Bi-NC) as a nanozyme for cancer therapy. The Bi-NC nanozyme displays both peroxidase (POD) and glutathione oxidase (GSHOx) biomimetic enzymatic activities, especially in a tumor microenvironment (TME), which catalyzes the production of hydroxyl radicals (·OH) and depletes antioxidant glutathione (GSH), simultaneously. Moreover, Bi-NC exhibits good photothermal conversion performance under near-infrared light irradiation. After surface modification with hyaluronic acid (HA) to improve the dispersity of nanoparticles and their accumulation in tumor tissues, Bi-NC@HA exhibits remarkable antitumor effects through the synergistic effect of catalytic and photothermal therapy. This work provides a new pathway for designing high-performance nanozymes for cancer catalytic therapy.

Introduction

In tumor tissues, the redox homeostasis of a tumor microenvironment (TME) has a substantial influence on tumorigenesis and the development and metastasis of tumors.[1,2] The level of reactive oxygen species (ROS) in tumors is generally higher than that in normal tissues, hence it can be used as a potential target for tumors.[3–5] In this decade, catalytic cancer therapy with the assistance of man-made nanozymes has become a research hotspot. In the TME, the nanozymes can catalyze local substrates to produce toxic substances, especially ROS, to directly kill cancer cells.[6–8] In cancer therapy, nanozymes have great advantages including high stability, low cost, high catalytic activity and good controllability.[9–13] Moreover, some nanozymes have many kinds of enzyme-like activities to catalyze cascade reactions, which can generate highly toxic ROS while destroying the antioxidant barrier, thus maximally disrupting the redox homeostasis in tumors and inducing cancer cell death.

Among various engineered nanozymes, metal-containing nanozymes, such as biomimetic natural metalloenzymes, have drawn great attention. The metal-containing nanozymes with metal active sites have shown outstanding performance in diverse catalytic reactions.[14–16] In particular, metal nanozymes are specifically responsive to a unique TME, including weak acidity and excessive production of hydrogen peroxide (H_2O_2) and glutathione (GSH). For instance, nanozymes with peroxidase (POD)-like enzyme activity can catalyze H_2O_2 to generate highly cytotoxic hydroxyl radicals (·OH), thereby enhancing cellular oxidative stress. A glutathione oxidase (GSHOx)-mimicking nanozyme can transform the reduced GSH into glutathione disulfide (GSSG), therefore reducing cell antioxidant capacities and ultimately assisting in enhancing the oxidative damage of cancer cells.[17–19]

Herein, aiming at the development of high-performance metal nanozymes, we have fabricated bismuth nanoclusters supported on nitrogen-doped porous carbon nanoparticles (Bi-NC) as the nanozyme for cancer therapy (Scheme 1). In response to excess H_2O_2 in the TME as well as a weakly acidic environment, Bi-NC possesses catalytic activities to produce the hydroxyl radical (·OH) and deplete glutathione (GSH), leading to severe cell oxidative stress and cell death. Moreover, Bi-NC has photothermal conversion properties that can synergize the catalytic reaction to improve the therapeutic results. It provides a practical paradigm for effective tumor nanocatalytic therapy.

[a]Beijing Institute of Nanoenergy and Nanosystems, Chinese Academy of Sciences, Beijing 101400, P. R. China. E-mail: lilinlin@binn.cas.cn
[b]School of Nanoscience and Engineering, University of Chinese Academy of Sciences, Beijing 100049, P. R. China
[c]Center on Nanoenergy Research, Guangxi University, Nanning, 530004, China
†Electronic supplementary information (ESI) available. See DOI: https://doi.org/10.1039/d3nr03957a
‡These authors contributed equally to this work.

Scheme 1 Schematic illustration of Bi-NC@HA for cancer therapy through synergetic catalytic and photothermal therapy.

Results and discussion

The synthetic process of Bi-NC is illustrated in Fig. 1a. Bi-NC was fabricated through a three-step method. The nitrogen-doped carbon nanoparticle (ZIF-NC) was derived from zeolitic imidazolate framework-8 (ZIF-8) *via* thermal calcination. Then, Bi nanoclusters were loaded onto the ZIF-NC scaffold by hydrothermal reaction to finally obtain Bi-NC. Scanning electron microscopy (SEM) and transmission electron microscopy (TEM) images revealed rhombic dodecahedron-shaped ZIF-NC with a size of approximately 130 nm and a narrow size distri-

Fig. 1 Synthesis and characterization of Bi-NC. (a) Synthetic procedure of Bi-NC. (b and c) TEM images of Bi-NC. (d) HRTEM image of Bi-NC. (e) EDS elemental mapping of Bi-NC (C, N, O and Bi). (f) XRD pattern of Bi-NC. (g) Raman spectra of Bi-NC and ZIF-NC. (h) High-resolution Bi 4f XPS spectrum of Bi-NC.

bution (Fig. S1†). It was observed that after loading the Bi nanoclusters, Bi-NC retained the pristine rhombic dodecahedron morphology of ZIF-8 (Fig. S2†). The TEM image of Bi-NC (Fig. 1b and c) revealed that metallic bismuth existing in the form of nanoclusters was evenly distributed surrounding the nanoparticles. The high-resolution TEM (HRTEM) (Fig. 1d) and electron diffraction images (Fig. S3†) indicated that the Bi nanoclusters were about 4.79 ± 0.5 nm with a d-spacing of 0.332 nm, corresponding to the (012) plane of metallic Bi. It should be noted that metal Bi is easily oxidized to +3 valence after exposure to air. As indicated in Fig. 1d (red), part of the nanoclusters was covered by an amorphous Bi_2O_3 nanolayer with a thickness of approximately 2 nm. Elemental analysis by energy dispersive X-ray spectroscopy (EDX) showed that the Bi element was uniformly distributed in Bi-NC especially at the outer surface of the NC (Fig. 1e). From the X-ray diffraction (XRD) pattern, the characteristic peaks of ZIF-8 were located at 7.35°, 10.37°, 12.76°, 16.49°, 18.07° and 22.16°, corresponding to the (011), (002), (112), (013), (222) and (114) crystal planes of ZIF-8, respectively (Fig. S4a†).[20] The XRD pattern of ZIF-NC after calcination showed two broad shoulder peaks located at around 25° and 44° (Fig. S4b†), which were assigned to the carbon (002) and (100)/(101) diffractions, respectively, suggesting the successful carbonization of ZIF-8. From the XRD pattern of Bi-NC (Fig. 1f), the main diffraction peak intensities and positions matched well with those of metallic Bi (PDF#44-1246), indicating the successful loading of Bi nanoclusters.

Subsequently, the structures of carbon in Bi-NC and ZIF-NC were investigated by Raman spectroscopy. As shown in Fig. 1g, the two scattering bands of Bi-NC and ZIF-NC were located at 1328 and 1575 cm^{-1}, corresponding to the D and G bands of carbon, respectively. The intensity ratios I_D/I_G of Bi-NC and ZIF-NC were calculated to be 1.105 and 1.085, respectively, suggesting the nature of defective amorphous carbon. The chemical composition and valence state of Bi-NC were further investigated by X-ray photoelectron spectroscopy (XPS) (Fig. S5a†). It should be noted that the peaks of 164.4 eV and 159.1 eV correspond to Bi $4f_{5/2}$ and Bi $4f_{7/2}$ of Bi^{3+}, respectively, confirming that Bi oxidized rapidly when exposed to air to form the Bi_2O_3 nanolayer on the Bi-NC surface (Fig. 1h). In addition, the N 1s spectrum of Bi-NC can be well deconvoluted into three peaks positioned at 397.2, 399.2, and 402.9 eV, suggesting that pyridinic N, pyrrolic N and graphitic N species coexisted (Fig. S5b†), which was also found in ZIF-NC (Fig. S6†). Furthermore, the Brunauer–Emmett–Teller (BET) surface area of Bi-NC was determined to be 825.24 m^2 g^{-1} and the pore volume was 1.318 cc g^{-1} (Fig. S7†). The large specific surface area and porous structure are conducive to the exchange of substances (*i.e.*, substrates, intermediates, and products) and exposure of active sites during the catalytic reactions.[21,22]

To improve the biocompatibility and *in vivo* circulation stability of Bi-NC, hyaluronic acid (HA) was employed to modify the surface of Bi-NC *via* electrostatic absorption, denoted as Bi-NC@HA. The resultant Bi-NC@HA showed

Fourier transform infrared spectral bands consistent with HA. The three peaks located at 1040, 1620 and 3425 cm^{-1} corresponded to the –O–, –COOH and –OH functional groups of HA, respectively, proving the successful modification of HA (Fig. S8†). The hydrodynamic diameter of Bi-NC@HA was about 200 nm and the zeta potential reversed from +31.4 to −27.4 mV after the surface modification (Fig. S9†). The negative zeta potential is more conducive to prolonging the blood circulation time of nanoparticles, so that the nanoparticles can avoid being opsonized by negatively-charged plasma proteins, and take advantage of the enhanced permeability and retention effect (EPR) to enhance their accumulation at tumor sites.[23,24] In addition, Bi-NC@HA was stable in different media and the average hydrodynamic size and polydispersity index (PDI) did not change significantly within 14 days (Fig. S9d and 9e†). These results indicated that Bi-NC@HA had good stability, which is helpful for long-term storage and application.

We evaluated the peroxidase-like activity of Bi-NC by the catalytic oxidation of 3,3′,5,5′-tetramethylbenzidine (TMB) in the presence of H_2O_2 (Fig. 2a). First, we investigated the POD-like activities of ZIF-NC and Bi-NC at different pH values (Fig. 2b and c). From the UV absorption spectra of oxidized TMB (oxTMB), both ZIF-NC and Bi-NC had POD-like activity and the enzymatic activity was enhanced with the decrease of pH from 7.4 to 4. The POD-like activity of Bi-NC was remarkably higher than that of ZIF-NC. In addition, the modification of HA did not adversely affect the catalytic activity. In fact, the catalytic activity of Bi-NC@HA was slightly enhanced and further improved under near-infrared light irradiation (Fig. S10a†). We performed methylene blue (MB) degradation experiments to confirm that Bi-NC@HA had excellent POD-like activity, which was further enhanced under near-infrared light irradiation (Fig. S10b†). The generation of ˙OH $(1:2:2:1)$ was verified using the electronic spin resonance (ESR) spectra using 5,5-dimethyl-1-pyrroline N-oxide (DMPO) as the trapping agent of ˙OH (Fig. 2d).

Although Bi-NC exhibited POD-like activity to catalyze the generation of highly toxic ˙OH, excessive GSH produced in cancer cells would rapidly deplete the produced ˙OH, which may lead to a reduction of therapeutic efficacy.[25] Therefore, we evaluated whether Bi-NC had GSHOx enzymatic activity to deplete GSH and disrupt antioxidant barriers within the tumor cells. After mixing various concentrations of Bi-NC with GSH, the remaining GSH was determined using 5,5′-dithiobis-(2-nitrobenzoic acid) (DTNB) based on the reaction of GSH with DTNB to produce TNB with typical absorbance at 412 nm. As shown in Fig. 2e, a decrease in the absorbance at 412 nm was observed as the concentration of Bi-NC increased, indicating that Bi-NC@HA had GSHOx-like activity to deplete GSH. The ability of Bi-NC@HA to oxidize GSH under the action of near-infrared light was further enhanced (Fig. S10c†).

From the diffuse reflectance UV-vis spectra, the optical absorption of ZIF-8 in the visible and near-infrared (NIR) regions was substantially enhanced after calcination and the absorption in the NIR region was not obviously changed after Bi loading (Fig. 2f–h). Therefore, we measured the near-infrared light absorption and photothermal conversion capacity of Bi-NC. As shown in Fig. 2i, the photothermal curve showed that the temperature of 200 μg mL^{-1} Bi-NC@HA dispersive solution increased from room temperature to 66 °C after 10 min of irradiation under 808 nm light (1 W cm^{-2}), and the temperature increase was positively correlated with the concentrations of Bi-NC@HA, proving that Bi-NC@HA had good photothermal conversion ability. Subsequently, Bi-NC@HA with a concentration of 200 μg mL^{-1} was subjected to 5 heating and cooling cycles of light irradiation. The maximum temperature of the Bi-NC@HA suspension was stable at around 66.2 °C, and the temperature drop during the five heating–cooling cycles was negligible, proving the good photothermal conversion stability (Fig. 2j). Through calculations, the photothermal conversion efficiency of Bi-NC was 35.34% (Fig. 2k and l). Therefore, Bi-NC can act as an outstanding photothermal agent for photothermal therapy (PTT) in the NIR region to induce local hyperthermia.

Encouraged by these excellent catalytic activities and the photothermal conversion capacity of Bi-NC@HA, the synergis-

Fig. 2 Enzyme-like activity and photothermal properties of Bi-NC@HA. (a) Diagram showing the detection of POD-like activity of Bi-NC@HA. (b) TMB absorption changes showing POD-like activity of ZIF-NC with the addition of H_2O_2 at various pH values. The inset shows the color of the solution after the reactions. (c) TMB absorption changes show POD-like activity of Bi-NC@HA with the addition of H_2O_2 at various pH values. The inset shows the color of the solution after the reactions. (d) EPR spectra of ˙OH trapped by DMPO under different conditions. (e) GSH consumption with different concentrations of Bi-NC@HA. The inset shows the color of the solution after the reactions. Diffuse reflectance UV-vis spectra of (f) ZIF-8, (g) ZIF-NC, and (h) Bi-NC. (i) Temperature increases with various concentrations of Bi-NC@HA. (j) Photothermal stability profile under NIR light irradiation. (k) Temperature change curve of Bi-NC@HA aqueous suspension. (l) Linear fitting curve of the cooling time of Bi-NC@HA as a function of negative logarithm of temperatures (τ_s is the time constant of the sample). Bi-NC@HA, 200 μg mL^{-1}.

Paper

tic therapeutic effect was explored at the cellular level. In most research studies, researchers evaluate the cytotoxicity of nanoparticles by adding a suspension of the nanoparticles to a cell culture medium with adherent cells (Fig. 3a). Under this condition, the cells will not sufficiently contact those nanoparticles well-dispersed in the cell culture medium. In contrast, if the nanoparticles have poor dispersion in the medium and tend to settle at the bottom of the culture over time, the local concentration of nanoparticles on the cell surface will be much higher than their initial bulk concentration, and they might be endocytosed into the cells, leading to visually increased cytotoxicity.[26,27] When studying the toxicity of our nanoparticles to the cells, we found that Bi-NC before surface modification rapidly sedimented at the bottom of the well plate, thus leading to high cytotoxicity to L929 cells, as demon-

strated by the methylthiazolyl tetrazolium (MTT) assay (Fig. S11†). After surface modification with HA, Bi-NC@HA can be uniformly and stably dispersed in the medium due to the greatly improved dispersibility. The MTT assay results showed that the L929 cells after being co-cultured with Bi-NC@HA at a concentration of 200 μg mL^{-1} for 24 hours had cell viability over 80%, proving the good biocompatibility of Bi-NC@HA (Fig. 3b).

Subsequently, the antiproliferative effect of Bi-NC@HA on breast cancer 4T1 cells was studied. The 4T1 cells were treated with different doses of Bi-NC@HA for 24 h, and then the cell viability was evaluated. It was found that when the concentration of Bi-NC@HA was increased to 200 μg mL^{-1} in acidified medium (pH = 6.5), significant proliferation inhibition with an inhibition rate of 49.2% was observed (Fig. 3c). In the neutral medium at a pH of 7.4, the cytotoxicity was significantly weakened. The tumor microenvironment is weakly acidic, and this acidic condition was more favorable for Bi-NC@HA to catalyze the generation of toxic ˙OH to kill the tumor cells. This result was consistent with the higher POD-like enzyme activity of Bi-NC@HA under acidic conditions *in vitro*. Interestingly, compared with the Bi-NC@HA group with 200 μg mL^{-1}, almost all the 4T1 cells died when irradiated with an 808 nm laser for 5 min subsequently. We also confirmed the result by live/dead cell staining with calcein acetoxymethyl ester (calcein-AM) and propidium iodide (PI) (Fig. 3d). In the Bi-NC@HA and Bi-NC@HA + laser groups, 37.5% and 98.5% of the cell died, respectively (Fig. 3e).

To observe the intracellular location of Bi-NC@HA after endocytosis, we labeled Bi-NC@HA with the fluorescent molecule fluorescein isothiocyanate (FITC) for fluorescence imaging. The 4T1 cells were co-cultured with FITC-linked Bi-NC@HA and endosomes/lysosomes were stained with LysoTracker RED. We found that Bi-NC@HA was located in the cells, partially co-localized with endosomes/lysosomes (exhibiting yellow fluorescence), and partially located in the cytoplasm (green fluorescence), proving that they can enter the cells by endocytosis and function after escaping from the cellular lysosomes into the cytosol (Fig. 3f).

Subsequently, the intracellular generation of ROS was confirmed using the cellular ROS probe 2,7-dichlorofluorescin diacetate (DCFH-DA). As shown in Fig. 3g, compared with the Bi-NC@HA group, stronger fluorescence was observed in the Bi-NC@HA + 808 nm group, indicating that the NIR light can significantly enhance the POD-like activity of Bi-NC@HA to elevate the intracellular ROS level. Compared with the laser group and the control group, the cellular ROS level in the Bi-NC@HA and Bi-NC@HA + laser groups increased by 6-fold and 21-fold, respectively (Fig. 3h). Therefore, the catalytic activity and PTT of Bi-NC@HA synergistically increased the production of ROS in 4T1 cells to improve the cancer cell killing.

Generally, the elevated cellular ROS level and cellular oxidative stress might induce apoptosis through the mitochondrial pathway, in which a change in the mitochondrial membrane potential and permeability occurs.[28,29] We used 5,5′,6,6′-
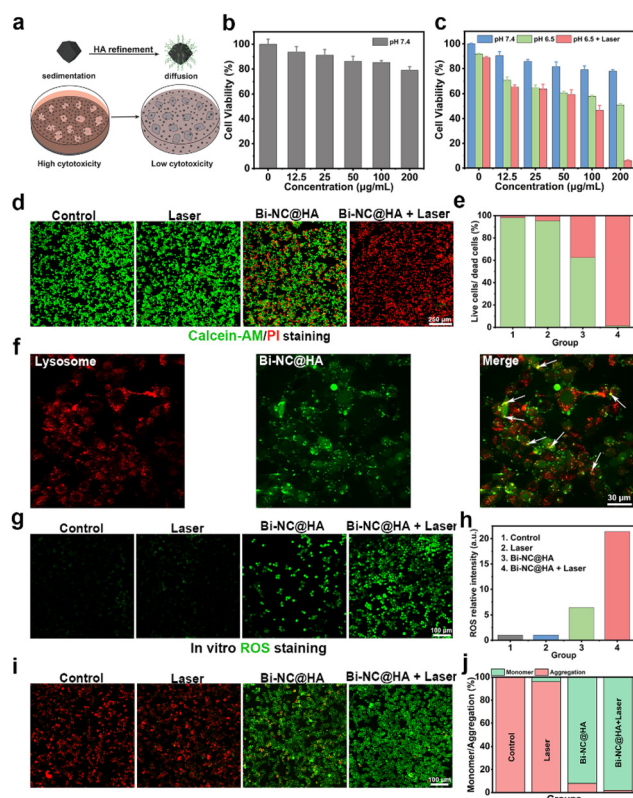
Fig. 3 Cytocompatibility and cancer cell killing of Bi-NC@HA. (a) Schematic diagram showing the effect of sedimentation and diffusion on cellular uptake of nanoparticles. (b) Cytotoxicity assessment of L929 cells. (c) Cytotoxicity assessment of 4T1 cells. 4T1 cells were treated with Bi-NC@HA (200 μg mL^{-1}) at pH 6.5. For NIR irradiation, an 808 nm laser at 1 W cm^{-2} was applied for 5 min. (d) Live/dead cell staining assay. 4T1 cells were co-stained with calcein-AM (green for live cells) and PI (red for dead cells). (e) The corresponding quantitative data. Dead cells in each group were counted from fields of view using Image J. (f) Confocal fluorescent images of the intracellular location of taken-up FITC-labeled Bi-NC@HA, co-stained with LysoTracker RED. (g) Detection of ROS generation with DCFH-DA after different treatments. (h) The corresponding ROS relative intensity of 4T1 cells after various treatments. (i) JC-1 staining of the 4T1 cells as an indicator of mitochondrial depolarization. The color shows JC-1 aggregates (red) and monomers (green). (j) Green/red FL ratios of the cells.

tetrachloro-1,1′,3,3′-tetraethyl-imidacarbocyanine iodide (JC-1) to stain the cell mitochondria, which is a mitochondrial probe that exhibits red fluorescence on normal mitochondrial membranes (from JC-1 aggregates), and green fluorescence on damaged mitochondrial membranes (from JC-1 monomers). The disruption of the mitochondrial membrane was observed with the treatment of Bi-NC@HA, which reduced the red fluorescence and increased green fluorescence. In the Bi-NC@HA + laser group, the red fluorescence of the cells almost disappeared, indicating a strong disruption of the mitochondrial membrane (Fig. 3i and j). These results confirmed that Bi-NC@HA-induced cell death was associated with mitochondrial membrane disruption and ROS production.

Prior to exploring the *in vivo* anti-tumor activity, the biocompatibility of Bi-NC@HA was assessed by a hemolytic assay and acute toxicity test through intravenous injection of the nanoparticles into mice. From the hemolytic test result, Bi-CN@HA at a concentration of up to 800 μg mL^{-1} still had an extremely low hemolysis rate of <3%, indicating its high hemocompatibility (Fig. S12a†). For evaluating the systematic acute toxicity, different doses of Bi-NC@HA (50, 100 and 200 mg kg^{-1}) were intravenously injected into mice. In the following 14 days, the mice had no abnormalities in activity, health status, food and water intake compared to those in the control group and the trend in body weight in the treatment group was similar to that in the control group (Fig. S12b†). On day 14 after intravenous administration, blood biochemical tests showed no abnormal changes in liver and kidney function indicators including alanine aminotransferase (ALT), aspartate aminotransferase (AST), creatinine (CREA) and blood urea nitrogen (BUN) in mice injected with Bi-NC@HA relative to the control group (Fig. 4a). From the routine blood tests, white blood cells (WBCs), red blood cells (RBCs), haemoglobin (HGB), platelets (PLTs), haematocrit (HCT), mean vascular volume (MCV), mean corpuscular hemoglobin (MCH), and mean corpuscular hemoglobin concentration (MCHC) were all within normal levels at different doses of Bi-NC@HA (Fig. 4b). Finally, hematoxylin and eosin (H&E) staining of the major organs including the heart, liver, spleen, lungs and kidneys showed no histological abnormalities in all mice (Fig. 4c). These results indicated the high biocompatibility of Bi-NC@HA *in vivo*.

After confirming the cancer cell-killing effect of Bi-NC@HA at the cellular level and its *in vivo* biocompatibility, we further investigated its *in vivo* anti-tumor effect. The procedures for handling the animals were according to the national standards "Laboratory Animal Requirements of Environment and Housing Facilities (GB 14925-2001)" and were approved by the Animal Ethics Committee of Beijing Institute of Nanoenergy and Nanosystems (approval number: 2021A041). The *in vivo* anticancer effect of Bi-NC@HA synergized with PTT was evaluated on the tumor-bearing mice. Briefly, BALB/c mice with subcutaneous 4T1 tumors were assigned into four groups (*n* = 6 in each group) and treated with (1) PBS, (2) laser, (3) Bi-NC@HA, and (4) Bi-NC@HA + laser. Bi-NC@HA (20 mg kg^{-1}) was intravenously injected into the mice, and NIR light (808 nm, 1.0 W cm^{-2}, 5 min) was locally irradiated at the tumor sites (Fig. 5a).

Fig. 4 *In vivo* systematic toxicity of Bi-NC in female ICR mice. (a) Blood biochemistry and (b) blood routine test on day 14 after i.v. injection of Bi-NC@HA with different doses (50, 100, and 200 mg kg^{-1}). (c) H&E staining of major organs (heart, liver, spleen, lungs and kidneys) of ICR mice after 14 days of intravenous injection of varying doses of Bi-NC@HA.

At 10 h post-injection of Bi-NC@HA, we directly observed that Bi-NC@HA with dark colors can target the tumor tissues through the EPR effect (Fig. 5b). The tumors of the mice treated with Bi-NC@HA were obviously blackened. The efficient tumor accumulation ensured that the subsequent NIR light irradiation could be imposed on Bi-NC@HA to synergize the therapy. In the Bi-NC@HA + laser group, during 5 min of NIR light irradiation, the maximum temperature at the tumor site increased to 57 °C when monitored using an infra-red camera (Fig. 5c). In contrast, in the PBS group, the maximum temperature at the tumor site was only 39 °C within 5 min of NIR light irradiation.

After the single therapy, the tumors in the PBS group grew fast, a moderate inhibition of tumor growth in the mice injected with Bi-NC@HA was observed, and the tumors in the Bi-NC@HA + laser group were remarkably inhibited with 3/6 of the mouse tumors having completely disappeared at the terminal of the therapeutic course (Fig. 5d and Fig. S13†). Compared with the PBS group and the laser group, the tumor inhibition rates of the Bi-NC@HA group and the Bi-NC@HA + laser group reached 50.59% and 95.14%, respectively (Fig. 5e). The final tumor weights and optical photographs of the resected tumors are shown in Fig. 5f and g. During 16 days of

Fig. 5 *In vivo* cancer therapy with Bi-NC@HA on subcutaneous 4T1-bearing mice. (a) *In vivo* treatment schedule with Bi-NC@HA. (b) Representative photographs of 4T1-tumor-bearing mice at 10 h after intravenous injection with Bi-NC@HA or PBS (right). (c) Localized tumor infrared imaging of the mice exposed to 808 nm NIR irradiation for 5 min. NIR light was imposed at 10 h after intravenous injection of Bi-NC@HA (PBS instead for only the NIR group) (n = 6 per group). (d) *In vivo* 4T1 tumor proliferation curves of the mice. (e) *In vivo* 4T1 tumor proliferation curves of the mice after various treatments. *P < 0.05, **P < 0.01, and ***P < 0.001, and n.s. for nonsignificant. (f) Tumor weight after dissection on day 16 of post-therapy. (g) Photographs of the dissected tumors on day 16 of post-therapy. The black circles indicate complete ablation of the tumors. Groups 1–4 represent groups of (1) PBS; (2) laser (1 W cm^{-2}, 5 min); (3) Bi-NC@HA (20 mg kg^{-1}); (4) Bi-NC@HA + laser. (h) Changes in body weights of the 4T1 tumor-bearing mice in different groups during the treatment. Values are presented as means ± s.d. (n = 6 per group). (i) Hematoxylin–eosin (H&E) and (j) Ki-67 immunohistochemical staining of the tumors after 16 days of various treatments.

treatment, there was no significant difference in the body weight change of the mice in each group, showing good biocompatibility (Fig. 5h). In addition, the hematoxylin and eosin (H&E) and Ki-67 immunohistochemical staining of the tumor sections showed that cancer cells in the Bi-NC@HA + laser group were severely reduced and a large proportion of necrosis area can be observed (Fig. 5i and j). Furthermore, all the major

organs of the mice (heart, liver, spleen, lungs, and kidneys) after therapy had normal tissue structures without pathological changes (Fig. S14†), demonstrating that the therapy is biosafe. It is worth mentioning that the dose of Bi-NC@HA for the therapy was only 1/10 of the safe dose in the evaluation of systematic toxicity, demonstrating the broad window of the treatment of Bi-NC@HA. To sum up, Bi-NC@HA synergized with PTT exhibited outstanding tumor growth inhibitory efficacy with good biosafety.

Conclusions

In conclusion, we have developed an innovative nanozyme of bismuth nanoclusters on nitrogen-doped porous carbon with favorable biocompatibility and high catalytic performance for cancer catalytic and photothermal therapy. The Bi-NC@HA nanozyme exhibited excellent dual POD- and GSHOx-like enzyme activities and photothermal conversion performance. Cellular experiments confirmed that Bi-NC@HA induced intracellular ROS elevation and mitochondrial damage, finally enhancing cancer cell death. The *in vivo* results also demonstrated that Bi-NC@HA after intravenous injection into mice achieved a substantial tumor inhibition with a tumor inhibition rate of 95.14% under NIR light irradiation. This work provides a promising strategy for designing high-performance metal nanozymes for cancer catalytic therapy.

Conflicts of interest

The authors declare no competing financial interest.

Acknowledgements

References

1 E. Panieri and M. Santoro, *Cell Death Dis.*, 2016, **7**, e2253–e2253.

2 B. Kumar, S. Koul, L. Khandrika, R. B. Meacham and H. K. Koul, *Cancer Res.*, 2008, **68**, 1777–1785.

3 W. Yin, W. Ke, W. Chen, L. Xi, Q. Zhou, J. F. Mukerabigwi and Z. Ge, *Biomaterials*, 2019, **195**, 63–74.

4 S. Wang, Z. Wang, G. Yu, Z. Zhou, O. Jacobson, Y. Liu, Y. Ma, F. Zhang, Z. Y. Chen and X. Chen, *Adv. Sci.*, 2019, **6**, 1801986.

5 M. Wu, Y. Ding and L. Li, *Nanoscale*, 2019, **11**, 19658–19683.

6 H. Wei and E. Wang, *Chem. Soc. Rev.*, 2013, **42**, 6060–6093.

7 L. Gao, J. Zhuang, L. Nie, J. Zhang, Y. Zhang, N. Gu, T. Wang, J. Feng, D. Yang and S. Perrett, *Nat. Nanotechnol.*, 2007, **2**, 577–583.

8 G. Tang, J. He, J. Liu, X. Yan and K. Fan, *Exploration*, 2021, **1**, 75–89.

9 L. Zhang, H. Wang and X. Qu, *Adv. Mater.*, 2023, 2211147.

10 W. Yang, X. Yang, L. Zhu, H. Chu, X. Li and W. Xu, *Coord. Chem. Rev.*, 2021, **448**, 214170.

11 H. Wei, L. Gao, K. Fan, J. Liu, J. He, X. Qu, S. Dong, E. Wang and X. Yan, *Nano Today*, 2021, **40**, 1016.

12 K. Fan, J. Xi, L. Fan, P. Wang, C. Zhu, Y. Tang, X. Xu, M. Liang, B. Jiang and X. Yan, *Nat. Commun.*, 2018, **9**, 1440.

13 H. Wang, K. Wan and X. Shi, *Adv. Mater.*, 2019, **31**, 1805368.

14 M. Wang, M. Chang, C. Li, Q. Chen, Z. Hou, B. Xing and J. Lin, *Adv. Mater.*, 2022, **34**, 2106010.

15 Y. Ai, Z. N. Hu, X. Liang, H. B. Sun, H. Xin and Q. Liang, *Adv. Funct. Mater.*, 2022, **32**, 2110432.

16 S. Zhong, C. Xiong, Y. Zhao, S. Yao, Q. Hu, S. Wang, Q. Zhao and L. Li, *Adv. Funct. Mater.*, 2023, 2305625.

17 Y. Li, Y. Zhang, Y. Dong, O. U. Akakuru, X. Yao, J. Yi, X. Li, L. Wang, X. Lou and B. Zhu, *Adv. Mater.*, 2023, 2210464.

18 D. Wang, H. Wu, C. Wang, L. Gu, H. Chen, D. Jana, L. Feng, J. Liu, X. Wang and P. Xu, *Angew. Chem.*, 2021, **133**, 3038–3044.

19 M. Chang, Z. Hou, M. Wang, C. Yang, R. Wang, F. Li, D. Liu, T. Peng, C. Li and J. Lin, *Angew. Chem., Int. Ed.*, 2021, **60**, 12971–12979.

20 Y. Pan, Y. Liu, G. Zeng, L. Zhao and Z. Lai, *Chem. Commun.*, 2011, **47**, 2071–2073.

21 Z. Zhao, Y. Long, S. Luo, Y. Luo, M. Chen and J. Ma, *J. Energy Chem.*, 2021, **60**, 546–555.

22 N. Singh, M. A. Savanur, S. Srivastava, P. D'Silva and G. Mugesh, *Angew. Chem.*, 2017, **129**, 14455–14459.

23 S. Honary and F. Zahir, *Trop. J. Pharm. Res.*, 2013, **12**, 255–264.

24 M. Dellian, F. Yuan, V. Trubetskoy, V. Torchilin and R. Jain, *Br. J. Cancer*, 2000, **82**, 1513–1518.

25 F. Cao, Y. Sang, C. Liu, F. Bai, L. Zheng, J. Ren and X. Qu, *ACS Nano*, 2022, **16**, 855–868.

26 E. C. Cho, Q. Zhang and Y. Xia, *Nat. Nanotechnol.*, 2011, **6**, 385–391.

27 T. M. Sager, D. W. Porter, V. A. Robinson, W. G. Lindsley, D. E. Schwegler-Berry and V. Castranova, *Nanotoxicology*, 2007, **1**, 118–129.

28 Y. Zhao, S. Wang, Y. Ding, Z. Zhang, T. Huang, Y. Zhang, X. Wan, Z. L. Wang and L. Li, *ACS Nano*, 2022, **16**, 9304–9316.

29 X.-L. Xu, N.-N. Zhang, G.-F. Shu, D. Liu, J. Qi, F.-Y. Jin, J.-S. Ji and Y.-Z. Du, *ACS Nano*, 2021, **15**, 19394–19194.